Available online at www.sciencedirect.com

ScienceDirect

Ceramics International 39 (2013) 9533–9547

CERAMICS INTERNATIONAL

www.elsevier.com/locate/ceramint

Ni-free, black ceramic pigments based on Co—Cr—Fe—Mn spinels: A reappraisal of crystal structure, colour and technological behaviour

Michele Dondi[a,*], Chiara Zanelli[a], Matteo Ardit[b], Giuseppe Cruciani[b], Luciana Mantovani[c], Mario Tribaudino[c], Giovanni B. Andreozzi[d]

[a]Institute of Science and Technology for Ceramics, CNR-ISTEC Faenza, Italy
[b]Department of Physics and Earth Sciences, University of Ferrara, Italy
[c]Department of Physics and Earth Sciences "Macedonio Melloni", University of Parma, Italy
[d]Department of Earth Sciences, Sapienza University of Rome, Rome, Italy

Received 6 April 2013; received in revised form 14 May 2013; accepted 15 May 2013
Available online 31 May 2013

Abstract

A reappraisal of crystal structure, optical properties and technological behaviour of black spinels in the Co—Cr—Fe—Mn system was carried out to define the best compositions and disclose the role of crystal chemistry in colouring performance and pigment-glaze interactions. Twenty ternary and quaternary spinel formulations were designed using crystallochemical criteria and prepared by simulating the industrial synthesis. Powder samples were characterized through X-ray diffraction (Rietveld), optical, Raman and Mössbauer spectroscopies, and technological testing in several glazes and glassy coatings. Black spinels fall in a relatively narrow field of unit cell and inversion parameters in between "chromites" and "magnetites". Their cation distribution is governed by Co^{2+} occupancy of tetrahedrally-coordinated site T and Cr^{3+} occupancy of octahedrally-coordinated site M, with Mn^{3+} hosted at M, while Mn^{2+} and Fe^{3+} are distributed over both sites. Nevertheless, Raman and Mössbauer spectra indicate a growing disorder in cation partitioning going towards the iron-rich terms. The pigment technological behaviour depends to a large extent on crystal chemistry of spinels, with no effect by grain or crystallite size. The best colouring performance corresponds to recommended compositions able to withstand corrosion and change in crystal chemistry in contact with melted glaze. Three different pathways can give rise to excellent black pigments: (a) strongly disordered spinels having an inversion parameter i~0.2; (b) moderately disordered spinels, free of Mn^{3+}, with $i < 0.1$; (c) apparently ordered and normal spinels halfway from cobalt chromite and cobalt ferrite. Poor technological performances are due to different conditions leaving room to colour bleaching (low Cr amount), glaze bloating (excess of Mn^{3+}) and limited resistance to corrosion (oversaturation of site M by Cr+Fe with formation of kenotetrahedral spinels or eskolaite—hematite solid solutions).

Keywords: Ceramic pigment; Crystal chemistry; Crystal structure; Mössbauer spectroscopy; Raman spectroscopy

1. Introduction

In ceramic decoration, black colour is obtained by using two kinds of pigment: eskolaite—hematite solid solutions $(Cr, Fe)_2O_3$ and complex spinel compositions in the Co—Cr—Fe—Mn—Ni—(Cu—V) system [1,2]. Since the eskolaite—hematite pigments are less stable in glazes [3,4], the most popular black colorants in the ceramic industry are based on the spinel structure [5,6].

Spinel oxides have general formula AB_2O_4 with A and B commonly being divalent (M^{2+}) and trivalent (M^{3+}) cations, and the oxygen sublattice forming a pseudo-cubic close packed arrangement. The unit cell of spinel (*Fd-3m* space group) contains 8 formula units (Z=8) consisting of 32 anions and 24 cations [7,8]; these latter occupy 8 tetrahedrally-coordinated (T site) and 16 octahedrally-coordinated interstices (M site). The cation occupancy at the T and M sites is usually expressed as

$$^{T}(A_{1-i}B_i)^{M}[A_iB_{2-i}]O_4$$

where i is the *inversion parameter* by which the spinel structure can assume two extreme configurations: *normal spinel* (i=0)

*Corresponding author. Tel.: +39 546 699728; fax: +39 546 46381.
E-mail address: michele.dondi@istec.cnr.it (M. Dondi).

0272-8842/$ - see front matter © 2013 Elsevier Ltd and Techna Group S.r.l. All rights reserved.
http://dx.doi.org/10.1016/j.ceramint.2013.05.072

typically hosts divalent (A) and trivalent (B) cations at the T and M sites, respectively; *inverse spinel* (i=1) typically hosts A cations at the M site and B cations half at the T site and half at the M site. A completely random distribution between T and M sites occurs when i=2/3; therefore, a spinel with $0 < i < 2/3$ is "largely normal" while another one with $2/3 < i < 1$ is "largely inverse" [8,9]. The inversion parameter is primarily affected by the temperature at which a given spinel is equilibrated, and secondarily by its chemical composition [9,10].

In the pigment industry, black spinels are designed by merging Co—Fe (CPMA code 13-39-9), Co—Cr—Fe (13-40-9), Fe—Mn (13-41-9) and Ni—Cr—Fe (13-50-9) systems [11]. Design criteria are empirical and based on cumulative light absorption by multiple chromophores. As the colour of pigments is the result of subtractive synthesis [12] and every chromophore has its own optical bands absorbing a given wavelength range, the concept is that gathering as many cations as possible will produce a total absorption in the visible spectrum. For *chromophore* is here intended a transition metal ion in a given ligand environment, as the same cation will have optical bands at different energy once octahedrally- or tetrahedrally-coordinated [13,14]. Such an approach is particularly effective in spinels, where the occurrence of transition elements with different valence states in octahedrally- and tetrahedrally-coordinated sites is rather common as a consequence of the partial or total inversion degree [7,8]. This circumstance provides extremely complex optical spectra where a number of bands, originated by *d-d* electronic transitions and metal—metal or metal—ligand charge transfer, almost completely filtre the visible light.

A further complication stems from the ceramic process, as pigments interact during firing with the matrix where they are dispersed, especially with the liquid phase formed at high temperature in glazes and bodies [15—17]. Such interactions may lead to pigment deterioration by different ways:

(i) Partial or total dissolution in the liquid phase [17,18].
(ii) Phase transformation, e.g. black $(Cr,Fe)_2O_3$ eskolaite—hematite will turn, once applied in Zn-rich glazes, into brown $Zn(Cr,Fe)_2O_4$ spinel [4,19,20].
(iii) Change of crystal chemistry with effect on coloration: a black $FeCr_2O_4$ spinel may turn, once applied in Zn-rich glazes, into a green $Zn(Cr,Fe)_2O_4$ one [21]; this phenomenon is especially active in spinels, which easily adjust their composition and inversion degree in function of temperature and chemical environment [22,23].

Despite the huge literature on spinels, just a limited number of papers have been devoted to complex compositions in the Co—Cr—Fe—Mn—Ni—V system used for black pigments, not considering the complicated stoichiometries stemming from the use of industrial residues [24—29]. Basic structural and technological results were achieved by Eppler [30,31] and by Lee et al. [32—35]. The synthesis practice has demonstrated that any deviation from spinel stoichiometry brings about the formation of hematite—eskolaite [30—34] that is deleterious for colouring performance (turning black into brown). The best technological behaviour in ceramic glazes is that of $Co_{1-x}Mn_xCr_{2-y}Fe_yO_4$ compositions where $0.4 < x < 1.0$ and $0.14 < y < 0.72$ with some nickel occasionally present [33—36]. In the case of Co-free pigments, the best behaviour in glaze applications is that of $Ni_{1-x}Mn^{2+}_xCr_{2-y-z}Fe_yMn^{3+}_zO_4$ spinels where $0.02 < x < 0.1$, $0.8 < y < 1.0$ and $0.02 < z < 0.08$ with sometimes a little addition of vanadium [30—32], copper [37] or magnesium and zinc [38].

Such a picture of black ceramic pigments, with well established industrial formulations, has been put in discussion in the latest years by both innovation in decoration technology — first of all inkjet printing [39—41] — and stricter health regulations. In order to fulfil the new requirements, important changes have been brought to particle size distribution, by moving towards submicrometric size [41,42], and composition of pigments, e.g. removing Ni from recipes [42,43]. Thus colorant manufacturers have been forced to a big effort to reformulate black pigments by a trial-and-error procedure that has turned evident the need of a better understanding of the role of spinel crystal chemistry and the effect of phenomena occurring during firing.

The main goal of the present study is to disclose the best composition in the Co—Cr—Fe—Mn system by reappraising crystal structure, optical properties and ceramic behaviour of black spinels. Such an approach is expected to shed light on pigment-glaze interactions affecting the final crystallochemical features after the ceramic process.

2. Experimental

2.1. Pigment design

Twenty ternary and quaternary spinel formulations encompassing the compositional space of Ni-free industrial black pigments were designed using crystal chemical criteria based on current knowledge on cation distribution in spinels [8,44]. Our guideline was the preference of each cation for a given site of the spinel lattice: for instance, the fraction of transition metal ion in the octahedrally-coordinated site is known to depend, among several factors, on the OSPE, i.e. the Octahedral Site Preference Energy [13]. The cations expected to occur in the system under investigation present an affinity for the sixfold-coordinated site in decreasing order: $Cr^{3+} > Mn^{3+} \sim Ni^{3+} \sim Co^{3+} > Co^{2+} \sim Fe^{2+}$; on the other hand, Mn^{2+} and Fe^{3+} exhibit a wide range of values, because they play essentially a passive role, occupying the T site and/or the M site according to the deficit left by competing cations [13,44,45]. The very high OSPE value of Cr^{3+} was used to formulate firstly pigments where chromium fully occupies the M site, in order to force Co, Fe and Mn ions to access the T site. This criterion was then relaxed by lowering progressively the Cr occupancy of the M site, leaving Co, Mn and Fe, tested in different ratios, to distribute over the T and M sites of spinel structure (Table 1). By this way, Fe-free (samples 2 and 5) and Cr-free (7 and 8) samples were prepared together with others where the sum Cr+Fe saturates the M site (4, 6, 11 and 16); the remaining samples are Mn-bearing ternary and quaternary systems.

Table 1
Stoichiometry of batch formulations of pigments and crystal chemistry of as-synthesized spinels on the basis of 3 cations per formula unit (T = tetrahedral site T; M = octahedral site M). Samples 20 and 21 are on the basis of four anions per formula unit including cation vacancies (□).

Sample	Stoichiometry of batch formulations	Crystal chemistry of as-synthesized spinels
1	$Mn_{0.5}\ Fe_{0.5}\ Cr_{2.0}\ O_4$	$^{T}(Mn^{2+}_{0.53}\ Fe^{2+}_{0.47})\ ^{M}[Cr^{3+}_{1.97}\ Fe^{3+}_{0.03}]\ O_4$
2	$Co_{0.5}\ Mn_{0.5}\ Cr_{2.0}\ O_4$	$^{T}(Co^{2+}_{0.5}\ Mn^{2+}_{0.5})\ ^{M}[Cr^{3+}_{2.0}]\ O_4$
3	$Co_{0.5}\ Fe_{0.5}\ Cr_{2.0}\ O_4$	$^{T}(Co^{2+}_{0.59}\ Fe^{2+}_{0.41})\ ^{M}[Cr^{3+}_{1.89}\ Fe^{3+}_{0.11}]\ O_4$
4	$Mn_{1.0}\ Fe_{1.0}\ Cr_{1.0}\ O_4$	$^{T}(Mn^{2+}_{0.746}\ Fe^{3+}_{0.254})\ ^{M}[Cr^{3+}_{1.000}\ Fe^{3+}_{0.746}\ Mn^{3+}_{0.254}]\ O_4$
5	$Co_{1.0}\ Mn_{1.0}\ Cr_{1.0}\ O_4$	$^{T}(Co^{2+}_{1.0})\ ^{M}[Cr^{3+}_{1.0}\ Mn^{3+}_{1.0}]\ O_4$
6	$Co_{1.0}\ Fe_{1.0}\ Cr_{1.0}\ O_4$	$^{T}(Co^{2+}_{1.0})\ ^{M}[Cr^{3+}_{1.0}\ Fe^{3+}_{1.0}]\ O_4$
7	$Co_{0.5}\ Fe_{2.0}\ Mn_{0.5}\ O_4$	$^{T}(Co^{2+}_{0.500}\ Mn^{2+}_{0.256}\ Fe^{3+}_{0.244})\ ^{M}[Fe^{3+}_{1.756}\ Mn^{2+}_{0.244}]\ O_4$
8	$Co_{1.0}\ Fe_{1.0}\ Mn_{1.0}\ O_4$	$^{T}(Co^{2+}_{1.0})\ ^{M}[Fe^{3+}_{1.0}\ Mn^{3+}_{1.0}]\ O_4$
10	$Co_{0.334}\ Mn_{0.333}\ Fe_{0.333}\ Cr_{2.0}\ O_4$	$^{T}(Co^{2+}_{0.39}\ Mn^{2+}_{0.28}\ Fe^{2+}_{0.23})\ ^{M}[Cr^{3+}_{1.92}\ Fe^{3+}_{0.08}]\ O_4$
11	$Co_{0.5}\ Mn_{0.5}\ Fe_{0.5}\ Cr_{1.5}\ O_4$	$^{T}(Co^{2+}_{0.50}\ Mn^{2+}_{0.44}\ Fe^{3+}_{0.06})\ ^{M}[Cr^{3+}_{1.50}\ Fe^{3+}_{0.44}\ Mn^{2+}_{0.06}]\ O_4$
12	$Co_{0.667}\ Mn_{0.667}\ Fe_{0.666}\ Cr_{1.0}\ O_4$	$^{T}(Co^{2+}_{0.67}\ Mn^{2+}_{0.12}\ Fe^{3+}_{0.21})\ ^{M}[Cr^{3+}_{1.00}\ Fe^{3+}_{0.46}\ Mn^{3+}_{0.33}\ Mn^{2+}_{0.21}]\ O_4$
13	$Co_{0.834}\ Mn_{0.833}\ Fe_{0.833}\ Cr_{0.5}\ O_4$	$^{T}(Co^{2+}_{0.84}\ Mn^{2+}_{0.26}\ Fe^{3+}_{0.06})\ ^{M}[Cr^{3+}_{0.50}\ Fe^{3+}_{0.80}\ Mn^{3+}_{0.64}\ Mn^{2+}_{0.06}]\ O_4$
14	$Co_{1.0}\ Mn_{0.5}\ Fe_{0.5}\ Cr_{1.0}\ O_4$	$^{T}(Co^{2+}_{1.0})\ ^{M}[Cr^{3+}_{1.0}\ Fe^{3+}_{0.5}\ Mn^{3+}_{0.5}]\ O_4$
15	$Co_{0.5}\ Mn_{1.0}\ Fe_{0.5}\ Cr_{1.0}\ O_4$	$^{T}(Co^{2+}_{0.50}\ Mn^{2+}_{0.46}\ Fe^{3+}_{0.04})\ ^{M}[Cr^{3+}_{1.00}\ Fe^{3+}_{0.46}\ Mn^{3+}_{0.50}\ Mn^{2+}_{0.04}]\ O_4$
16	$Co_{0.5}\ Mn_{0.5}\ Fe_{1.0}\ Cr_{1.0}\ O_4$	$^{T}(Co^{2+}_{0.50}\ Mn^{2+}_{0.36}\ Fe^{3+}_{0.14})\ ^{M}[Cr^{3+}_{1.00}\ Fe^{3+}_{0.86}\ Mn^{2+}_{0.14}]\ O_4$
17	$Co_{0.87}\ Mn_{0.26}\ Fe_{0.87}\ Cr_{1.0}\ O_4$	$^{T}(Co^{2+}_{0.87}\ Fe^{3+}_{0.13})\ ^{M}[Cr^{3+}_{1.00}\ Fe^{3+}_{0.74}\ Mn^{3+}_{0.13}\ Mn^{2+}_{0.13}]\ O_4$
18	$Co_{0.75}\ Mn_{0.375}\ Fe_{0.375}\ Cr_{1.5}\ O_4$	$^{T}(Co^{2+}_{0.75}\ Mn^{2+}_{0.15}\ Fe^{3+}_{0.10})\ ^{M}[Cr^{3+}_{1.500}\ Fe^{3+}_{0.276}\ Mn^{3+}_{0.124}\ Mn^{2+}_{0.100}]\ O_4$
19	$Co_{0.375}\ Mn_{0.75}\ Fe_{0.375}\ Cr_{1.5}\ O_4$	$^{T}(Co^{2+}_{0.375}\ Mn^{2+}_{0.600}\ Fe^{3+}_{0.025})\ ^{M}[Cr^{3+}_{1.500}\ Fe^{3+}_{0.350}\ Mn^{3+}_{0.125}\ Mn^{2+}_{0.025}]\ O_4$
20	$Co_{0.375}\ Mn_{0.375}\ Fe_{0.75}\ Cr_{1.5}\ O_4$	$^{T}(Co^{2+}_{0.364}\ Mn^{2+}_{0.364}\ Fe^{3+}_{0.182}\ \square_{0.090})^{M}[Cr^{3+}_{1.455}\ Fe^{3+}_{0.545}]O_4$
21	$Co_{0.75}\ Fe_{0.75}\ Cr_{1.5}\ O_4$	$^{T}(Co^{2+}_{0.728}\ Fe^{3+}_{0.182}\ \square_{0.090})^{M}[Cr^{3+}_{1.455}\ Fe^{3+}_{0.545}]O_4$

In *italic* compositions recalculated to account for the occurrence of eskolaite—hematite solid solution.

2.2. Pigment synthesis

Reagent-grade Co_3O_4, Cr_2O_3, Fe_2O_3 and Mn_2O_3 were used. Batches of 10 g were wet mixed in porcelain jar with acetone then pelletized in a cylindric steel mould without any binder (pressure ~50 MPa). Pellets were fired in sealed alumina crucibles in electric furnace (static air, 3 °C min^{-1} to 1300 °C, 12 h soaking then natural cooling). Three samples containing eskolaite—hematite together with spinel were fired again with the same schedule, but in reducing atmosphere (96%Ar+4%H, flux 4 L min^{-1}) in order to increase the spinel amount. Fired pellets were crushed and ground in agata mortar until everything passed through a 63 μm sieve. Grain size distribution was determined by photosedimentation (Micromeritics, SediGraph 5000) on ground pigments, that overall exhibit a median diameter between 5 and 14 μm. Samples 4, 6, 7, 8, 13, 16, 20 and 21 were affected by an appreciable degree of sintering, thus resulting in a coarser grain size (on average between 15 and 25 μm). Some samples are attracted by a magnet and their magnetization degree decreases in the order: 7 > 8 ~ 13 > 6 > 4.

2.3. X-ray diffraction

X-ray powder diffraction measurements were carried out using two Bruker D8 Advance diffractometers: one equipped with a Si(Li) solid-state detector set to detect Cu $K\alpha_{1,2}$ radiation, operating in the 5—130°2θ angular range, 0.015°2θ scan rate, and 10 s per step counting time; the other equipped with a 1-dimensional LynxEye detector based on silicon strip technology, set to discriminate Cu $K\alpha_{1,2}$ radiation, in the 10—80°2θ measuring range, with an equivalent counting time of 16 s per 0.02°2θ step. Structural refinements were performed by the Rietveld method using the GSAS-EXPGUI software package [46,47] in the space group *Fd*-3*m* with origin set at -3*m*, starting from the model of Lenaz et al. [22]. The presence of associated eskolaite—hematite solid solution, detected only for samples 1, 3 and 10, was accounted for by carrying out multiphase refinements in which only the scale factors and the cell parameters were varied, except for spinel. The diffraction peak profiles were modeled by a pseudo-Voigt function one Gaussian (GW), and the two Lorentzian (i.e., LX, and LY, respectively) broadening coefficients plus an asymmetry contribution. Besides the 18 shifted Chebyshev polynomial coefficients to reproduce the background, the refinements included a scale factor, the cell parameter (a), T and M site occupancies, the oxygen coordinate (u), and isotropic atomic displacement parameters (U_{iso}). Cations hosted in the same coordination site were constrained to maintain the chemical composition and to change the isotropic temperature factors identically. Quantitative phase analysis of pigments applied in glazes was performed by internal standard addition (spiking) and Rietveld refinement technique using Topas 4.2 software (Bruker). The glazes (Table 2) containing samples 5, 6, 7, 8, 11, 12 and 13 were admixed with 20 wt% corundum, used as internal standard. Up to 50 independent variables were refined: phase fractions, zero point, 15 coefficients of the shifted Chebyschev function to fit the background, unit cell parameters, profile coefficients (one Gaussian, GW, and one Lorentzian term, LX). The agreement indices, as defined in Topas, for the final least-squares cycles of all refinements were in the following ranges: $2.0\% < R_p < 2.8\%$, $2.0\% < R_{wp} < 4.0\%$ and $1.0\% < GOF < 1.5\%$. The experimental error is within 5% relative.

Crystallite size was estimated through the Scherrer equation using mean FWHM of spinel peaks and assuming a cubic

Table 2
Glassy coatings (F1, F5) and glazes (S1, S2, S3) used in technological testing: chemical composition, physical properties and firing schedules.

Component/Property	Unit	F1	F5	S3	S2	S1
SiO_2	wt %	63.9	59.0	49.7	51.1	53.5
ZrO_2		< 0.1	< 0.5	8.1	< 0.1	< 0.1
B_2O_3		11.7	2.0	2.4	1.2	< 0.1
Al_2O_3		9.5	9.0	19.7	22.6	25.2
RO		0.5	14.0	16.0	16.3	12.3
R_2O		7.2	5.0	3.5	3.2	8.6
ZnO		1.0	11.0	< 0.1	5.1	< 0.1
PbO		5.5	< 0.5	< 0.1	0.9	< 0.1
Maturing temperature, T_m	°C	930	1010	1100	1150	1210
Viscosity at T_m	kPa s	4.90	4.28	5.24	4.97	4.65
Surface tension at T_m	mN m^{-1}	293	363	383	394	378
Refractive index	1	1.503	1.546	1.561	1.547	1.526
Coeff. thermal expansion, $a_{20—400\ °C}$	MK^{-1}	4.96	6.21	4.97	5.54	6.83
Maximum firing temperature	°C	1000	1050	1140	1170	1210
Firing cycle (cold-to-cold)	min	54	57	61	62	65
Soaking at maximum temperature	min	5	5	5	5	5

RO: alkaline-earth oxides (ΣMgO+CaO+SrO+BaO). R_2O: alkali oxides ($\Sigma Li_2O+Na_2O+K_2O$).

Table 3
Phase composition and crystal structural data of as synthesized spinels: unit cell parameters; metal—oxygen distances in tetrahedral (T—O) and octahedral (M—O) sites; bond angles, agreement factor of Rietveld refinement, and crystallite size.

Samples	Phase composition		Unit cell parameter, a (Å)		Oxygen parameter, u (adim.)		T—O distance (Å)		M—O distance (Å)		T—O—M bond angle (deg)		M—O—M bond angle (deg)		Agreement factor	Crystallite size (nm)
	Spinel	$(Cr,Fe)_2O_3$	mean	sd	mean	sd	mean	sd	mean	sd	mean	sd	mean	sd	RF^2	
1	93.04	6.97	8.39970	0.00122	0.26400	0.00040	2.022	0.006	1.990	0.003	120.48	0.15	96.55	0.19	0.0368	29
2	100.00	0.00	8.38573	0.00008	0.26311	0.00013	2.006	0.002	1.993	0.001	120.79	0.05	96.14	0.06	0.0172	85
3	81.61	18.39	8.34819	0.00054	0.26383	0.00029	2.007	0.004	1.978	0.002	120.53	0.11	96.48	0.14	0.0699	36
4	100.00	0.00	8.45443	0.00008	0.26229	0.00015	2.010	0.002	2.015	0.001	121.08	0.05	95.75	0.07	0.0335	94
5	100.00	0.00	8.37722	0.00012	0.26278	0.00018	1.999	0.003	1.993	0.001	120.91	0.07	95.98	0.09	0.0366	128
6	100.00	0.00	8.37704	0.00011	0.26042	0.00019	1.965	0.003	2.011	0.001	121.75	0.07	94.86	0.09	0.0302	84
7	100.00	0.00	8.45539	0.00030	0.25802	0.00026	1.948	0.004	2.048	0.002	122.58	0.09	93.73	0.12	0.0881	60
8	100.00	0.00	8.41822	0.00017	0.25923	0.00023	1.957	0.003	2.030	0.002	122.16	0.08	94.30	0.11	0.0585	83
10	82.89	17.11	8.39130	0.00054	0.26555	0.00030	2.043	0.004	1.976	0.002	119.91	0.11	97.30	0.14	0.0925	83
11	100.00	0.00	8.40623	0.00006	0.26232	0.00014	1.999	0.002	2.003	0.001	121.07	0.05	95.76	0.07	0.0198	149
12	100.00	0.00	8.41287	0.00014	0.25965	0.00019	1.962	0.003	2.025	0.002	122.01	0.07	94.50	0.09	0.0399	70
13	100.00	0.00	8.41703	0.00008	0.25876	0.00018	1.950	0.003	2.033	0.001	122.33	0.06	94.08	0.09	0.0319	86
14	100.00	0.00	8.37361	0.00008	0.25917	0.00021	1.946	0.003	2.020	0.002	122.18	0.07	94.27	0.10	0.0406	82
15	100.00	0.00	8.43032	0.00006	0.26223	0.00017	2.004	0.003	2.010	0.001	121.10	0.06	95.72	0.08	0.0267	88
16	100.00	0.00	8.41598	0.00008	0.26090	0.00017	1.981	0.002	2.016	0.001	121.57	0.06	95.09	0.08	0.0287	151
17	100.00	0.00	8.39268	0.00008	0.26000	0.00017	1.963	0.003	2.018	0.001	121.89	0.06	94.67	0.08	0.0285	154
18	100.00	0.00	8.38351	0.00006	0.26184	0.00015	1.987	0.002	2.002	0.001	121.24	0.05	95.54	0.07	0.0245	82
19	100.00	0.00	8.42100	0.00008	0.26295	0.00014	2.012	0.002	2.002	0.001	120.85	0.05	96.06	0.07	0.0235	142
20	100.00	0.00	8.38187	0.00012	0.26037	0.00017	1.965	0.003	2.012	0.001	121.76	0.06	94.84	0.08	0.0358	85
21	100.00	0.00	8.34139	0.00008	0.25933	0.00017	1.941	0.003	2.011	0.001	122.12	0.06	94.35	0.08	0.0311	145

shape ($k=0.94$). The instrumental broadening was accounted for by measuring LaB_6 as a reference material.

Because of their consecutive atomic number ($Z=24$, 25, 26, and 27 for Cr, Mn, Fe, and Co, respectively) the cation distribution between T and M sites was pursued through a constrained minimization (i.e., the range of compositional variation was kept close to that imposed by the nominal crystal chemistry). As reported in several works, differences between measured and calculated parameters can be minimized by a function $f(x)$ which considers different observed variables such as a, u, T and M occupancies [8,48]. A least-squares minimization was performed using the modified version of the MINUIT program as reported in Lavina et al. [8].

Phase composition, lattice parameter, oxygen coordinate, as well as tetrahedral and octahedral bond distances and angles, are listed in Table 3. Furthermore, the Rietveld refinement plot

for the sample with nominal composition (Co,Mn)Cr_2O_4 (i.e. sample 2) is reported in Fig. 1.

2.4. Mössbauer spectroscopy

For samples 11, 20, 13 and 16, characterized by increasing iron content (Table 1), the chemical state of iron and its coordination were investigated by ^{57}Fe Mössbauer spectroscopy using a conventional spectrometer operated in constant acceleration mode with a ^{57}Co source of nominal 50 mCi in rhodium matrix. Absorbers were prepared by pressing finely ground samples with a powdered acrylic resin (transoptic powder) to self-supporting discs. For the different samples, the amount of powder used was variable so as to have absorbers with Fe thickness of 2 mg/cm^2. From 3 to 6 million counts were collected to have good statistics. Spectra were recorded at room temperature within a velocity range from −10 to +10 mm/s, and the signal was transmitted to a multi-channel analyser. Data analysis involved a curve-fitting procedure made by assuming a Lorentzian peak shape and employing the fitting program Recoil 1.04. The statistical best fit was obtained by using the reduced χ^2 method and uncertainties were estimated on the basis of the covariance matrix. The experimental uncertainties were estimated to be about $\pm$0.03 mm/s for centre shift (CS) and quadrupole splitting (QS) as well as for the peak width at half maximum, $\pm$0.7 T for magnetic field (H), and $\pm$4% for absorption areas.

2.5. Raman spectroscopy

Raman spectroscopy was performed on polished samples 1 to 13 using a Jobin-Yvon Horiba LabRam microRaman apparatus. Several spectra were taken for each sample using as excitation source both the red 633 nm line of a He—Ne laser and the blue 473 nm line of a solid state Nd:YAG laser. The lower wavelength laser was used to minimize the fluorescence from Cr. A filter wheel reduced the laser power to 1 mW or less on the sample. The frequency calibration was performed against the Raman peak of silicon. Spatial resolution was ~1 μm, whereas spectral resolution was ~1.5 cm^{-1} for the 633 nm source, and 2.5 cm^{-1} for the 473 nm one. No attempt was done to measure oriented crystals. The peak positions were obtained from baseline-corrected spectra by least-squares spectral peak curve fitting using the computer program Labspec. A Lorentzian profile was used in the peak profile analysis. At least 5 spectra were collected from each sample in different positions, and with different wavelengths. The results obtained by the different emission sources are comparable; however the effect of fluorescence was lower than expected, and the use of a blue laser proved necessary only in samples 1 and 2. In the other samples, due to inherent lower resolution of the 473 nm laser, only the results for the red source are reported.

2.6. Technological behaviour

Optical features were analyzed by diffuse reflectance spectroscopy (DRS) on both as-synthesized pigments (powdered) and on pigment-bearing glassy coatings and glazes (after firing) by a Hunterlab MSXP4000 Miniscan spectrophotometer. As no individual optical band is discernible in the spectra, due to the almost complete light absorbance in the UV—visible range, only colourimetric CIE $L^*a^*b^*$ coordinates were determined (white glazed tile reference x=31.5 and y=33.3, illuminant D_{65}, 10° observer). These coordinates express brightness (L^*100=white, 0=black) and chroma: $+a^*$=red, $-a^*$=green; $+b^*$=yellow, $-b^*$=blue; $C^*=(a^{*2}+b^{*2})^{0.5}$. In order to get the purest black colour, minimal values of L^* and C^* are the target. High quality industrially-manufactured black pigments were taken as benchmark: spinels Sp1 (Co,Cr,Fe,Mn)$_3O_4$ and Sp2 (Co,Cr,Fe,Ni,Mn)$_3O_4$ as well as eskolaite—hematite EH (Cr,Fe)$_2O_3$.

Colouring performance was tested by wet mixing the pigment (5 wt%) in raw glaze that was laid as a button (∅ 4 cm) on a suitable ceramic substrate. Five different glazes and glassy coatings were tested, each with its proper firing schedule that is summarized together with composition and physical properties in Table 2. Colourimetric parameters were statistically elaborated by

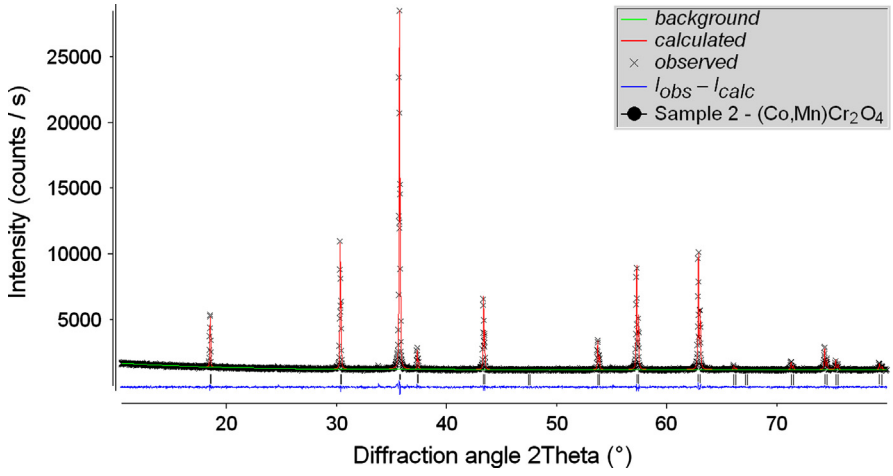

Fig. 1. Final Rietveld fit for the (Co,Mn)Cr_2O_4 sample (i.e. sample 2). The experimentally observed data are indicated by crosses (black), the calculated pattern is the continuous line (red), and the lower curve (blue) is the weighted difference between the calculated and observed patterns. Vertical ticks mark the position of reflections for the spinel phase (grey). (For interpretation of the references to color in this figure legend, the reader is referred to the web version of this article).

drawing contour plots where a 3-dimensional surface—contrasting chroma (C^*) with crystal chemistry of spinels—is represented on a 2-dimensional map with constant C^* lines (Statistica 7.1, surface fit by distance-weighted least-squares). Selected samples were further analyzed in order to get amount and unit cell parameter of spinel by XRD (see Section 2.3): the coating was mechanically removed, ground in agate mortar and admixed with an internal reference material (corundum, 20 wt%). The amount of residual spinel in the finished product, directly proportional to the corrosion resistance in melted glazes and glassy coatings during the ceramic firing, is here expressed as P, i.e. the pigment persistence (in percentage): $P\ (\%) = 100(S_f/S_i)$, where S_i is the initial concentration of spinel in the raw glaze (5 wt%) and S_f is the final concentration of spinel in the fired glaze (determined by XRD).

3. Results and discussion

3.1. Phase composition and crystal structure

All the analyzed powders are exclusively composed of one phase with spinel structure-type, with the only exception of samples 1, 3, and 10, where an eskolaite—hematite solid solution was detected (ranging from 7 to 18%, see Table 3). On the basis of literature data on the unit-cell parameters of eskolaite and hematite end-term structures [49—53], the associated solid solutions were estimated to be $Cr_{0.88}Fe_{0.12}O_3$, $Cr_{0.87}Fe_{0.13}O_3$, and $Cr_{0.84}Fe_{0.16}O_3$ for samples 1, 3, and 10, respectively.

Although having a great compositional heterogeneity, the synthesized samples reveal a mild variation of the spinel structural features, with the lattice parameter a that ranges from 8.34 to 8.46 Å, and the oxygen coordinate u comprised in between 0.258 and 0.266 (Table 3). In Fig. 2 the oxygen coordinates are plotted as a function of the cell parameters; furthermore, the fields of variation have been added—as obtained from the Inorganic Crystal Structure Database—for the following end-terms: Co-chromites ($CoCr_2O_4$), chromites ($FeCr_2O_4$), Mn-chromites ($MnCr_2O_4$), Co-ferrites ($CoFe_2O_4$), magnetites ($FeFe_2O_4$), and jacobsites ($MnFe_2O_4$). Fig. 2 clearly shows that the synthesized spinel compounds have structural parameters which fall in between "chromites" and "magnetites", and that their distribution is mainly related to the chromium content at the octahedrally-coordinated site. The incorporation of chromium induces a contraction of the octahedral bond lengths and, simultaneously, an elongation of the tetrahedral bond lengths, i.e., M—O varies from 2.048 to 1.976 Å and T—O from 1.941 to 2.043 Å going towards the chromite field (Fig. 3). It should be noted that both samples 5 and 8 lie outside the above-described trends. This fact can be readily explained by considering the high amount of sixfold-coordinated Mn^{3+}, which provokes an unexpected contraction of the lattice parameter and an elongation of the tetrahedral bond lengths (cation distribution will be further discussed in Section 3.4).

The spinel crystallite sizes range approximately from 30 to 150 nm with most pigments in between 70 and 95 nm (Table 3). No correlation exists between the dimension of crystallites and the pigment grain size. The smallest crystallites (~30 nm) are found in "chromites" coexisting with eskolaite—hematite (samples 1 and 3).

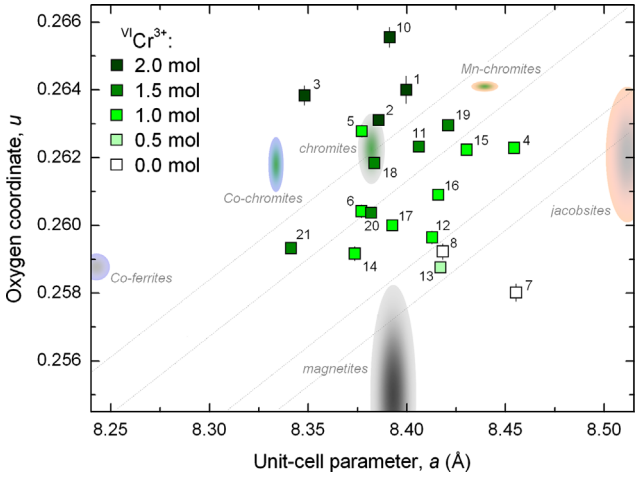

Fig. 2. Oxygen coordinate (u) as a function of the unit-cell parameter (a) variation. The colored areas refer to the fields of variation for the end-term spinel structures as extracted from the ICSD database.

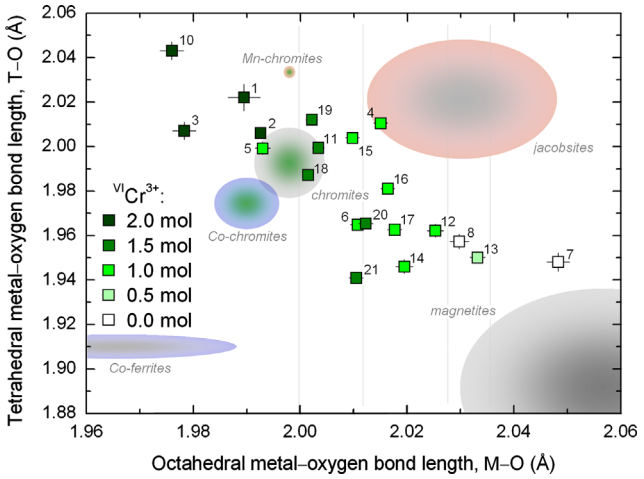

Fig. 3. Octahedral (M—O) vs. tetrahedral (T—O) mean bond distances. The colored areas refer to the fields of variation for the end-term spinel structures as extracted from the ICSD database.

3.2. Mössbauer spectra

Representative Mössbauer spectra of spinel samples are shown in Fig. 4. Sample 11, the Fe-poorest of the four analysed, shows a typical paramagnetic spectrum made of two doublets with hyperfine parameters Centre Shift (CS) of 0.36 mm/s and Quadrupole Splitting (QS) of 0.42 and 0.68 mm/s. Such values may easily be interpreted as ferric iron in octahedral coordination. Starting from sample 20 (through the Fe-richest samples 13 and 16), the Fe signal is confirmed to be due to ferric iron, but the Mössbauer spectrum becomes very complex, because several magnetic sextets are superimposed to the doublets and the internal magnetic field (H) is quite different from what expected. As for example, sample 20 shows two doublets (CS = 0.33 and 0.28 mm/s, QS = 0.50 and 1.89 mm/s, respectively) and at least

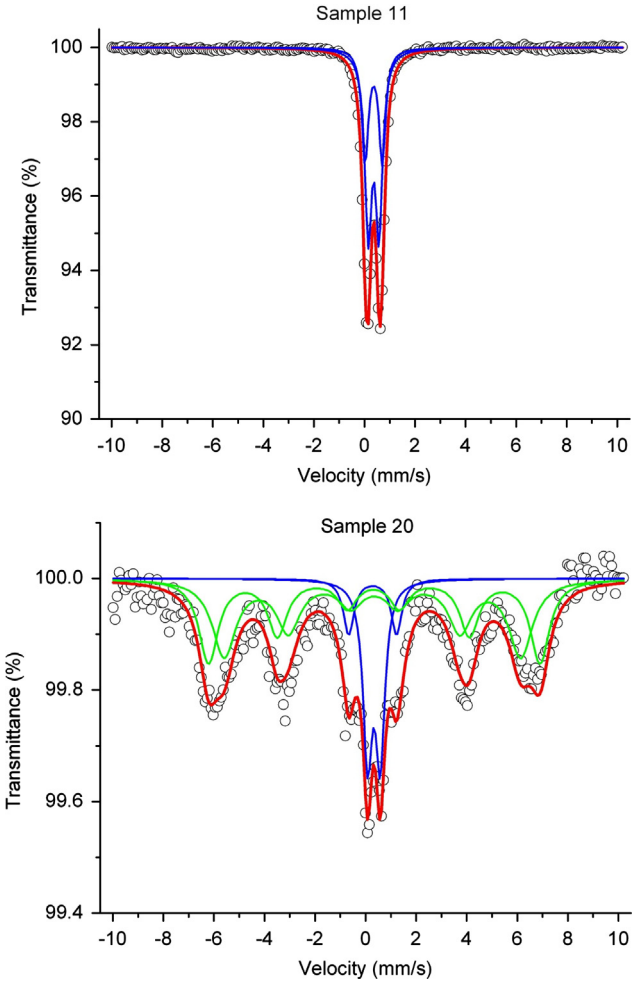

Fig. 4. Representative room temperature Mössbauer spectra of spinel samples. Circles = experimental spectrum, red thick line = calculated spectrum, internal blue lines = Fe^{3+} paramagnetic doublets, external green lines = Fe^{3+} magnetic sextets. (For interpretation of the references to color in this figure legend, the reader is referred to the web version of this article).

two sextets (CS = 0.33 and 0.30 mm/s), with these latter characterised by anomalously low *H* values (41 and 36 T, respectively) and representing 75% of the absorption spectrum. Notably, magnetic spectra represent up to 90% of the absorption in the spectra of samples 13 and 16. Such spectra are somewhat interpreted as due to relaxation phenomena, i.e., a magnetic behaviour which is manifested by nanosized iron oxide species (i.e. clusters or nanoparticles≤10 nm), but this explanation cannot apply to the present case because the spinel samples here investigated have crystallite size estimated between 85 and 151 nm (Table 3). An alternative explanation is that the Fe is increasingly incorporated but not homogeneously distributed into the spinel structure, this leading to a number of local arrangements richer in Fe and diluted in a spinel matrix poorer in Fe. This would be not evidenced by X-ray diffraction because the spinel general symmetry is not broken, but may be evidenced by Mössbauer spectroscopy which is sensitive to local order and to next-nearest-neighbours interactions. In addition to local arrangements, Fe disorder between T and M sites may be invoked for samples 20, 13 and 16.

3.3. Raman spectra

Group theory analysis predicts for spinels 5 Raman active peaks, with different symmetries [54]. In the $MgAl_2O_4$ spinel their frequencies are 311 (T_{2g}), 410 (E_g), 492 (T_{2g}), 671 (T_{2g}) and 772 (A_{1g}) cm^{-1}, respectively. In other spinels significant changes in peak position are observed with composition, but the same pattern is found [55]. However, already in the pioneering work by O'Horo et al. [54], extra peaks were observed (reported as "excess high frequency structure") in synthetic spinel with a slight amount of impurities. The additional peaks are due to the interaction of coexisting cations in the T and M sites, each of them with an effect on the Raman spectrum, in solid solutions or in the presence of cation site inversion. The violation of group theory predictions occurs because in the case of cation disorder the local symmetry decreases, and the number of permitted peak increases consequently [56,57]. Another effect of cation disorder is peak

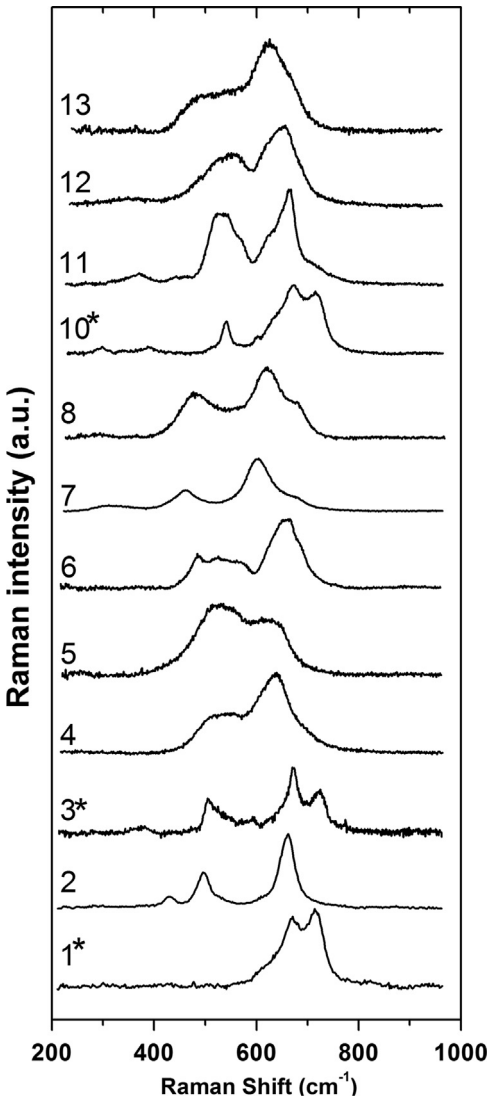

Fig. 5. Raman spectra of samples 1 to 13. The spectra were taken using the 633 nm laser, apart for samples 1 and 2, taken with the 473 nm laser source; *: samples with eskolaite—hematite.

broadening [58,59], which also occurs when small sized particles are present [60].

This explains the highly disordered nature of our Raman spectra, that show as a rule very broad, hardly resolvable peaks (Fig. 5). The presence of ternary and quaternary solid solutions, and of an inversion between tetrahedral and octahedral site cations in $FeMn_2O_4$ prompt for a decrease in local symmetry and the appearance of extra peaks.

There are however significant differences between the examined samples, which can then be divided in three groups:

(1) samples showing only peaks which are predicted by group theory for ordered cubic spinels. They are samples 2 and 7, that show single well resolved peaks, but broader in sample 7, and samples 1 and 10 that show much broader peaks, though still resolvable in a doublet of between 600 and 700 cm^{-1}; in sample 10 also the eskolaite peak at 549 cm^{-1} is apparent;
(2) samples 3, 6 and 11 that show several new peaks beyond group theory predictions, but still resolved; the new peaks are likely related to cation disorder;
(3) samples 4, 5, 8, 12 and 13 show very broad, hardly resolvable peaks and shoulders; in this case disorder and extreme peak broadening are observed. These samples contain octahedral Mn^{3+}, which is expected to give a significant Jahn—Teller distortion.

Within the above distinction, Raman spectra obtained from different analytical spots in the same sample commonly differ in peak position, intensity and broadening (Fig. 5). In fact only in the $(Co_{0.5}Mn_{0.5})Cr_2O_4$ spinel (sample 2) a homogeneous texture is observed.

Positions of the resolvable peaks and broadening of the peak at ~660 cm^{-1}, which can be measured in all samples, are reported in Table 4. The position of the 660 cm^{-1} peak was related to the reciprocal of the mass square root of the cation in the octahedral site (Fig. 6) in agreement with the attribution to octahedral vibration in spinel [61,62]. This peak is quite large in all the samples; for a comparison in natural spinel its width is about 27 cm^{-1}. Although expected for the above-mentioned cation disorder, such peak is extremely broad and diffuse in some samples. A possible reason is the occurrence of nano-sized particles, though the spinels under investigation never approach a diameter below 10 nm [60]. As shown in Fig. 7, these samples are all containing Mn^{3+}, although peak broadening is unrelated to the actual Mn^{3+} content. Local site distortion due to Jahn—Teller effect is suggested to have some effect in promoting the observed disorder.

3.4. Crystal chemistry

The calculated crystal chemistry of as-synthesized spinels is characterized by an overall pattern of cations distribution where Co^{2+} is exclusively in tetrahedral coordination and Cr^{3+} is always in octahedral coordination; as a consequence, both exhibit site occupancies corresponding to the nominal batch stoichiometry (Table 1 and Fig. 8). In contrast, iron and manganese occur in both T and M sites as divalent and/or trivalent ions. Manganese is present either as Mn^{2+} partitioning over T and M sites, or Mn^{3+} occupying only the M site by 0.12—1.0 atoms per formula unit (apfu), or both. Divalent manganese is mainly tetrahedrally-coordinated (from 0.12 to 0.75 apfu) as its occurrence in sixfold coordination is at most 0.24 apfu. Iron is present essentially as Fe^{3+}, as indicated by the Mössbauer spectroscopy, being preferentially hosted at the octahedrally-coordinated site, where its occupancy is in the 0.28—1.76 apfu range; fourfold coordinated Fe^{3+} has a maximum concentration as high as 0.25 apfu. The occurrence of Fe^{2+} is claimed to justify the composition of samples 1, 3 and 10 fired under reducing atmosphere, where the predominant occurrence of chromium at site M imposed that the T site be accessed only by divalent ions. The composition of these

Table 4
Raman shift of main peaks and linewidth of the peak occurring at about 660 cm^{-1} (the only peak that can be followed along the series).

Samples	Raman shift (cm^{-1})								Peak at ~660 cm^{-1} linewidth (cm^{-1})
1						620	672	718	53
2	429	497					660		35
3	370	505	527	586			671	723	29
4			526				634		77
5			530				633		60
6		485	529	569			655		52
7	316	461					602	668	55
8	447			560			622	677	75
10	296	339	386		540	634	673	717	52
11	367		450	517	544	635	665	705	32
12	349				541		650		62
13			486		540		627		79

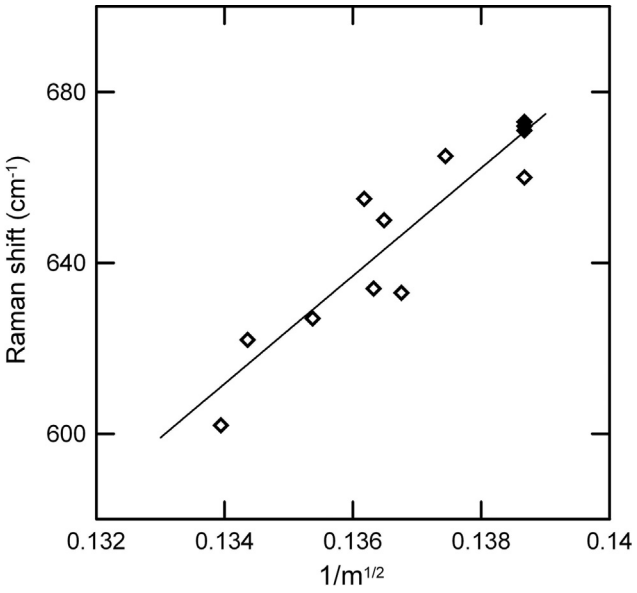

Fig. 6. Raman Shift of the peak at ~660 cm^{-1} vs. the inverse of the square mass of the octahedral cation ($1/m^{1/2}$).

spinels was recalculated taking into account the amount of eskolaite—hematite; some Fe^{3+} (or Mn^{3+}) are allowed to access the octahedrally-coordinated site (Table 1).

On the whole, the cation distribution in the spinels under investigation fulfils the models proposed in the literature [8,44,45,55,63]. Unexpectedly, two samples (20 and 21) do not match this crystal chemical pattern: as in these spinels the octahedrally-coordinated M site is saturated by trivalent chromium and iron ions, only divalent ions should be accommodated at the tetrahedrally-coordinated T site. However, the Mössbauer spectroscopy carried out on sample 20 excludes the presence of Fe^{2+}, and the measured short T—O distances strongly support the occurrence of Fe^{3+} at the T site. This may happen provided that a defective "kenotetrahedral" cation arrangement occurs, i.e., with extra-Fe^{3+} in T site accompanied by cation vacancy (□) in a 2:1 proportion [64]. Such phenomenon was proved to account for natural and artificial oxidation of spinels by several studies [65, and references therein]. In addition, it was shown by the latter authors that the presence of Cr^{3+} at the M site has a strong stabilisation effect on tetrahedrally-coordinated vacancy, because this latter assumes a "soft" behaviour as a function of the predominant cation at the M site (the ^{T}□-O distance was 2.000 Å for ^{M}Cr, 2.030 Å for $^{M}Fe^{3+}$, and 2.056 Å for ^{M}Al+Cr).

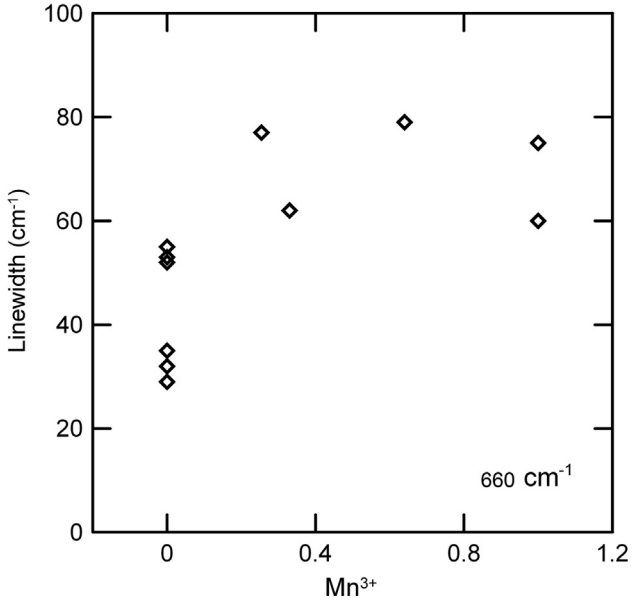

Fig. 7. Linewidth of the peak at ~660 cm^{-1} vs. Mn^{3+} content (apfu).

These trends in spinel crystal chemistry have relevant consequences on pigment formulation: it is relevant the role played by Cr^{3+} and Co^{2+} as scaffolding to force Fe^{3+}, Mn^{2+} and Mn^{3+} into the remaining vacant sites. Where the nominal sum Cr+Fe is $\gg 2$ apfu (i.e. the M site is oversaturated), it is not possible to turn, in industrial-like synthesis conditions, the excess of Fe^{3+} into Fe^{2+} that would have an OSPE value low enough to ease its access into the tetrahedrally-coordinated site. As a consequence, a secondary phase (eskolaite—hematite solid solution) is formed, in agreement with previous works [30—34]. This occurs even after firing in reducing atmosphere, though it is able to lower the amount of eskolaite—hematite in samples 1, 3 and 10 from 30 to 50% (firing under oxidizing atmosphere) to 8—18% (reducing atmosphere).

However, it seems to exist a threshold for Fe in excess, not mentioned before in the literature. As a matter of fact, an excess of Fe^{3+} in the batch as high as 0.25 apfu did not bring about the exsolution of eskolaite—hematite, likely giving rise to a kenotetrahedral cation arrangement (samples 20 and 21), whereas an excess of 0.31 apfu did form the associated phase (sample 10).

Partitioning of Fe and Mn over the two sites of spinel is stressed when the nominal sum Cr+Fe+Mn exceeds 2 apfu. This circumstance occurred in ten samples (4, 7, 11, 12, 13, 15, 16, 17, 18 and 19); all of them exhibit a remarkable degree of disorder, intended as the occurrence of Mn^{2+} and Fe^{3+} in both tetrahedral and octahedral coordination, implying an inversion parameter $0.02 < i < 0.25$. Such a disorder is particularly pronounced, as well outlined by Raman spectroscopy, in five samples out of ten (12, 13, 15, 18 and 19) where sixfold-coordinated Mn^{3+} accompanies the twice coordination of Mn^{2+} and Fe^{3+} ions.

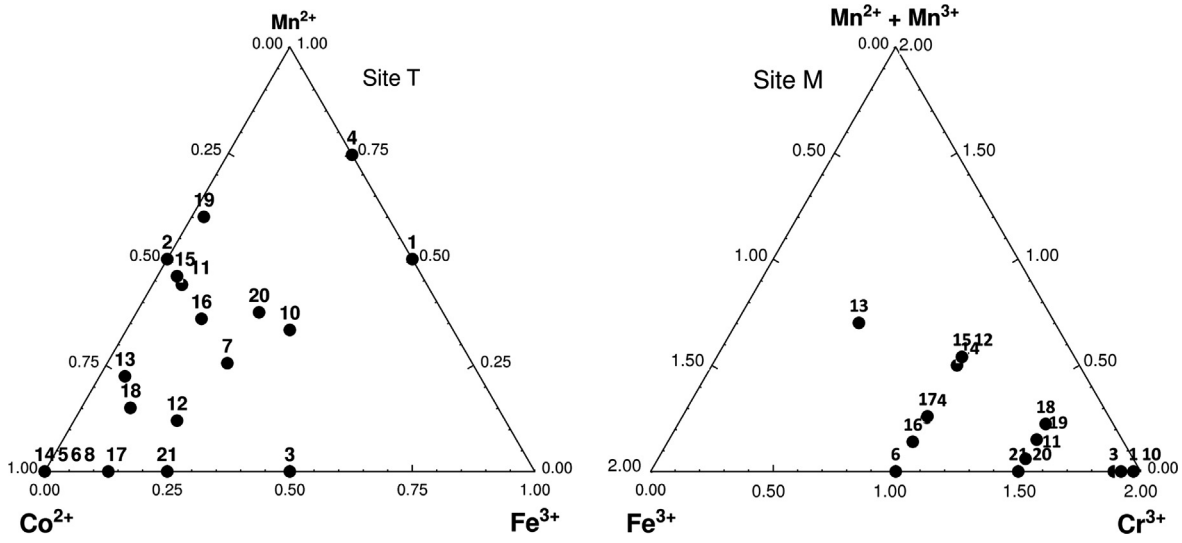

Fig. 8. Crystallochemical composition of as-synthesized spinels (samples 1, 3 and 10 contain Fe^{2+} instead of Fe^{3+} at site T).

3.5. Technological behaviour

3.5.1. As-synthesized pigments

As-synthesized pigments exhibit a deep black colour with very low brightness, $38.6 < L^*_{as} < 40.5$, and chroma, $0.2 < C^*_{as} < 1.2$ (Table 5). Exception is done for three pigments that appear distinctly bluish-green (sample 2: a^*—12.8, b^*—2.0) or dark brown (sample 1: a^* 4.8, b^* 3.1 and to a minor extent sample 4: a^* 1.8, b^* 1.1). These "out-of-target" results were somehow expected, as sample 2 is a sort of cobalt chromite—that is a common blue-green pigment [2,3]—and samples 1 and 4 are cobalt-free chromites typically characterized by brown shades [24—27].

3.5.2. Technological tests

Technological tests evidenced that black colour does not depend on pigment grain size or dimension of spinel crystallites. There are different behaviours, along with "out-of-target" colours, in various glazes and glassy coatings used in ceramic tile production (Fig. 9):

- Deep black pigments that are more or less stable in the various coatings under investigation; the best behaviour is on average that of samples 12, 11 and 6 which display colour coordinates ($28 < L^*_{av} < 30$ and $C^*_{av} \leq 0.6$) matching those of the best industrially-manufactures spinels, including Ni-bearing formulations (Table 5).
- Three samples underwent colour bleaching, turning into dark gray shades (samples 7, 8 and 10).
- Three black pigments (samples 5, 8 and 13) induced bloating, a phenomenon provoking swelling and blistering of glaze or glassy coating [66].

These behaviours may be related to the spinel capacity to withstand the corrosion by melted glaze. This is reflected by pigment persistence P (Table 6) that was determined for the best black samples (6, 11 and 12) as well as for bleached (7 and 8) and bloated samples (5, 8 and 13). The amount of residual spinel after firing, here assessed for the first time in the literature, varies widely from 18% to 100%. This range overlaps that determined for the $YAlO_3$:Cr perovskite pigment [18], although spinel pigments have a better persistence.

3.5.3. Best behaviour in ceramic applications

Contour plots were drawn in order to disclose the best pigment compositions by contrasting average chroma (C^*_{av}) with crystal chemistry of spinels. In particular, the Cr^{3+} occupancy of octahedral site and the Co^{2+} occupancy of tetrahedral site are plotted for various glazes and glassy coatings (Fig. 10). Most samples are black as synthesized and behave satisfactorily in low temperature applications (up to 1000 °C, e.g. in the transparent coating F1). They correspond to a wide compositional range, encompassing a Cr^{3+} occupancy from 0 to

Table 5
Brightness (L^*) and chroma (C^*) of as synthesized pigments and pigment-bearing glazes and glassy coatings. Uncoloured glazes (coating) and high-quality industrial pigments (Sp1, Sp2, EH) are reported as reference. B indicates the occurrence of glaze bloating (blt).

Sample	As-synthesized pigments		Glassy coatings				Glazes						Average colouring performance				
			F1		F5		S3		S2		S1						
	L^*_{as}	C^*_{as}	L^*_{F1}	C^*_{F1}	L^*_{F5}	C^*_{F5}	L^*_{S3}	C^*_{S3}	L^*_{S2}	C^*_{S2}	L^*_{S1}	C^*_{S1}	L^*_{av}	a^*_{av}	b^*_{av}	C^*_{av}	blt
Coating			*85.4*	*8.8*	*91.4*	*4.7*	*92.5*	*2.7*	*89.5*	*5.0*	*81.7*	*7.4*					
1	40.5	5.7	36.7	10.9	35.6	8.7	42.6	12.3	36.1	9.6	36.0	9.2	37.4	5.6	8.4	10.1	
2	48.2	13.0	38.1	12.1	38.5	14.0	43.0	15.0	38.6	11.1	36.6	15.0	38.9	−13.1	−2.9	13.4	
3	39.8	0.7	28.4	1.7	33.1	1.9	36.7	2.9	31.7	1.0	31.0	2.6	32.2	−1.9	0.1	1.9	
4	40.8	2.1	26.5	3.1	29.5	2.6	35.6	4.9	29.8	2.7	30.2	3.5	30.3	2.3	2.4	3.3	
5	40.0	0.6	27.1	0.6	31.6	0.7	31.0	1.1	28.6	0.6	28.4	1.3	29.3	0.1	−0.5	0.5	B
6	39.5	0.5	25.6	0.5	30.0	0.5	31.5	1.7	28.5	0.5	26.1	1.0	28.3	0.4	−0.5	0.6	
7	38.6	0.8	34.3	0.3	44.2	1.2	47.8	3.4	33.1	3.9	30.4	2.3	38.0	−1.1	−1.7	2.0	
8	40.0	0.2	25.6	0.8	40.9	4.5	39.4	7.6	28.6	4.1	26.8	3.0	32.3	0.2	−4.0	4.0	B
10	40.4	0.5	29.8	2.0	32.8	1.7	36.8	2.2	32.1	1.6	31.7	3.1	32.6	−1.3	1.3	1.8	
11	40.2	0.2	26.4	1.2	31.3	0.9	33.2	0.3	29.6	1.1	28.1	0.9	29.7	0.2	0.4	0.5	
12	39.6	0.2	25.4	1.0	30.4	1.4	33.1	0.3	29.8	0.5	28.3	1.0	29.4	0.2	0.2	0.3	
13	39.3	0.9	27.7	1.0	33.5	1.2	32.6	0.9	31.9	0.9	28.4	0.8	30.8	0.3	0.4	0.6	B
14	40.1	0.5	32.5	0.3	32.1	3.3	38.1	5.7	29.0	2.4	26.5	1.9	31.6	0.2	−2.7	2.7	
15	39.9	0.3	31.5	0.4	30.7	2.4	36.4	3.1	28.6	1.4	26.9	1.0	30.8	0.4	−1.6	1.6	
16	40.1	0.7	29.9	0.6	31.1	1.9	37.5	2.9	29.0	1.0	26.7	1.1	30.8	0.3	−1.4	1.5	
17	39.3	0.3	32.7	0.6	31.5	2.2	37.9	4.6	28.8	1.8	25.8	1.5	31.4	0.2	−2.0	2.0	
18	39.1	0.9	29.9	0.2	31.5	2.2	37.7	3.9	29.2	1.5	27.1	0.8	31.1	0.0	−1.7	1.7	
19	39.7	0.4	30.0	0.4	32.0	2.3	38.8	2.7	29.5	1.0	26.6	0.8	31.4	0.3	−1.4	1.4	
20	39.5	0.5	35.0	1.1	31.1	1.9	37.9	1.9	29.5	0.7	27.4	0.6	32.2	0.6	−1.0	1.1	
21	39.5	1.2	31.3	0.3	29.9	2.2	35.6	3.1	28.9	1.0	26.6	1.2	30.5	0.2	−1.5	1.5	
Sp1			24.0	0.2	28.1	1.0	32.3	1.6	27.7	0.5	26.3	0.3	27.7	0.0	−0.5	0.5	
Sp2			29.0	0.6	28.8	1.4	32.1	1.9	28.0	0.8	25.8	0.5	28.7	0.3	−0.6	0.7	
EH			25.0	1.0	33.1	10.5	39.9	19.6	32.2	12.8	30.3	9.8	32.1	8.2	6.8	10.7	

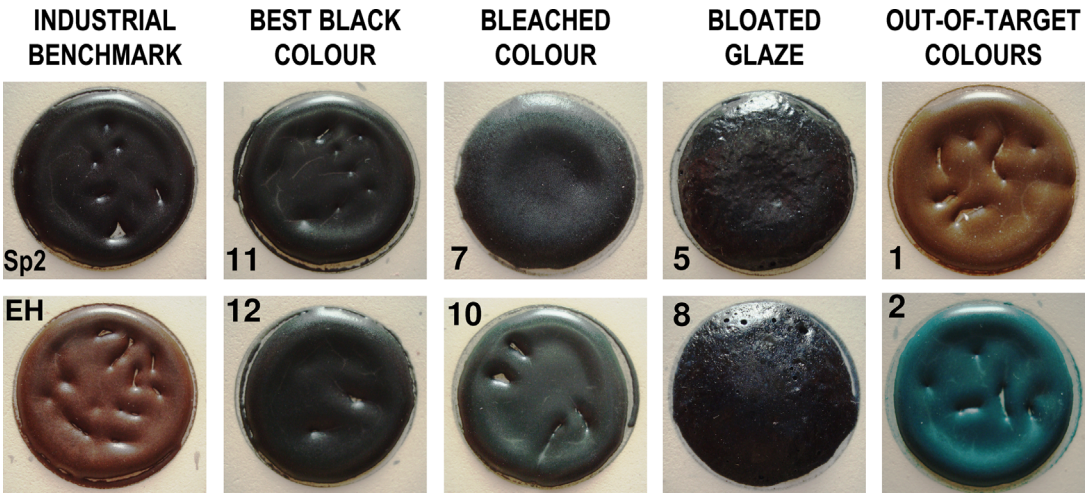

Fig. 9. Example of technological behaviour of spinel pigments applied in glaze S1.

Table 6
Unit cell parameter and persistence of spinel pigment after firing at 1050 °C (glassy coating F5) or 1200 °C (glaze S1).

Sample	Unit cell parameter a (Å)			Pigment persistence		Coating type
	As-synthesized, a_{as}	After firing, a_{af}	Difference, $a_{as}-a_{af}$	Amount after firing (wt%)	P (%)	
5	8.377	8.351	0.026	2.3 ± 0.1	46	S1
6	8.377	8.364	0.012	4.0 ± 0.1	80	S1
7	8.455	8.433	0.022	2.4 ± 0.1	48	F5
8	8.422	8.410	0.012	0.9 ± 0.1	18	F5
11	8.403	8.360	0.043	4.8 ± 0.1	96	S1
12	8.404	8.363	0.041	5.0 ± 0.1	100	S1
13	8.415	8.380	0.035	3.8 ± 0.1	76	S1

Standard deviation of the unit cell length is < 0.001 Å in the as-synthesized spinels and ~ 0.001 Å after firing.

1.6 apfu and a Co^{2+} occupancy from 0.2 to 1.0 apfu. However, this picture rapidly evolves in typical glazes for porous wall tiles (S3), stoneware tiles (S2) and porcelain stoneware tiles (S1) which require increasing firing temperatures (up to ~1200 °C). The best behaviour is related to a smaller field that excludes both low and high degrees of Co^{2+} and Cr^{3+} occupancy at the sites T and M, respectively, as calculated by average colour coordinates (Fig. 11). The best technological behaviour—responsible for the best colouring performance—is shown by samples 6, 11 and 12, which display the deepest black colour and a very good resistance to corrosion (from 80% to 100%, distinctly better than the other spinels). The explanation of a different persistence has to be looked for by revising the composition of spinels. Overall, the best behaviour corresponds to a crystal chemistry where the tetrahedrally-coordinated site is mainly occupied by Co^{2+} (0.4—0.8 apfu) together with Mn^{2+} (0.1—0.5) and Fe^{3+} (0.1—0.25), and the octahedrally-coordinated site is predominantly occupied by Cr^{3+} (0.9—1.5 apfu) together with Fe^{3+} (0.3—1.0), Mn^{3+} (0.1—0.5) and Mn^{2+} (≤0.21). This picture adds substantial pieces of information to the current knowledge on black pigments [1—6,30—38]:

(i) by outlining that a remarkable complexity affects cation distribution in ternary and quaternary spinel pigments beyond that expectable from natural spinels;
(ii) by correcting the extension of compositional fields for the best technological performance of pigments: shifting downward the recommended concentrations of $^{IV}Mn^{2+}$ and $^{VI}Cr^{3+}$ and upward those of $^{IV}Co^{2+}$, $^{VI}Fe^{3+}$ and $^{VI}Mn^{3+}$.

Three different pathways are envisaged to get deep black shades:

(a) strongly disordered spinels, characterized by very broad and hardly resolvable Raman peaks and occurrence of magnetic sextets in Mössbauer spectra, hosting at least 7 transition metal cations and having an inversion parameter i~0.2 (e.g., sample 12);
(b) moderately disordered spinels, exhibiting several Raman peaks beyond the Group Theory prediction but a typical paramagnetic Mössbauer spectrum, being free of Mn^{3+} and having an inversion parameter $i < 0.1$ (e.g., sample 11);
(c) apparently ordered and normal spinels halfway from cobalt chromite and cobalt ferrite showing clues of disorder by extra

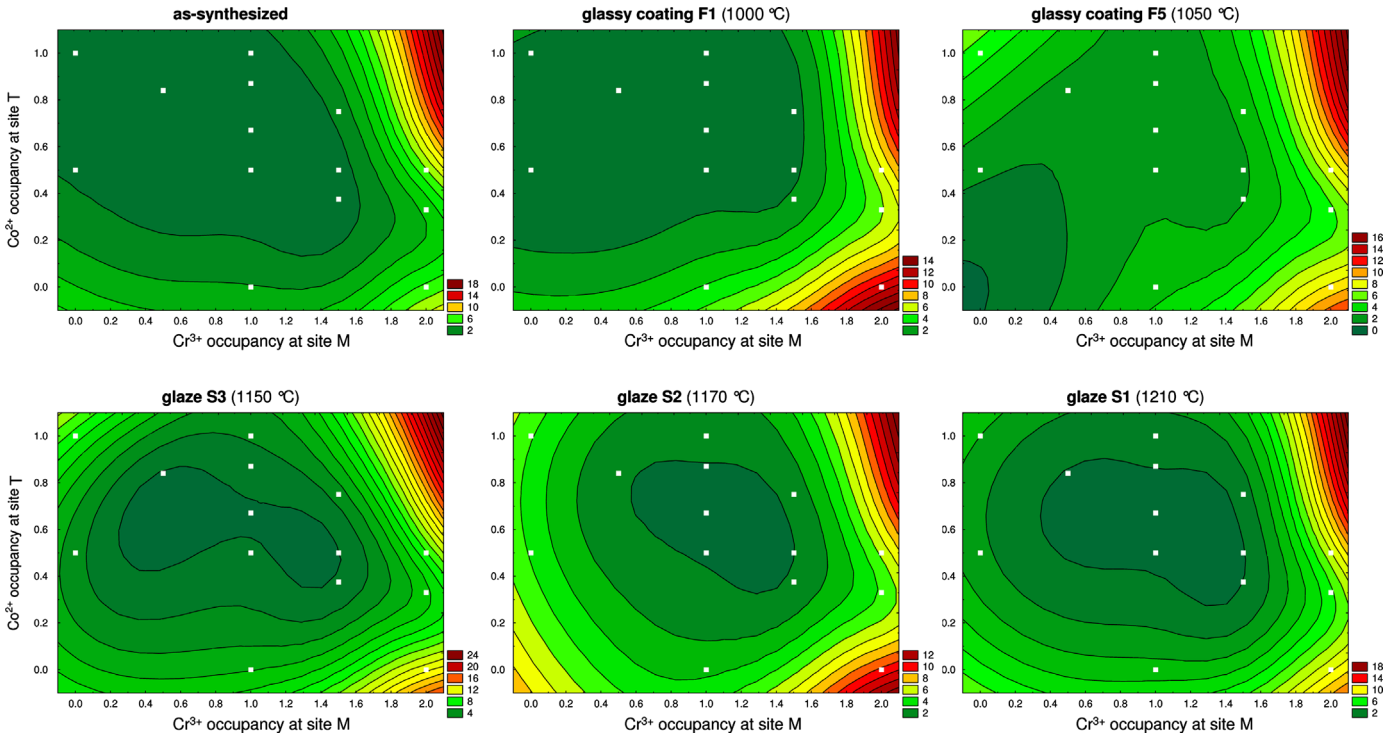

Fig. 10. Contour plots of chroma (C^*) versus spinel crystal chemistry for as-synthesized pigments and applied into different glazes and glassy coatings. Compositions with the best technological behaviour plot in the dark gray field (dark green in the online version). White squares represent the composition of samples. (For interpretation of the references to color in this figure legend, the reader is referred to the web version of this article).

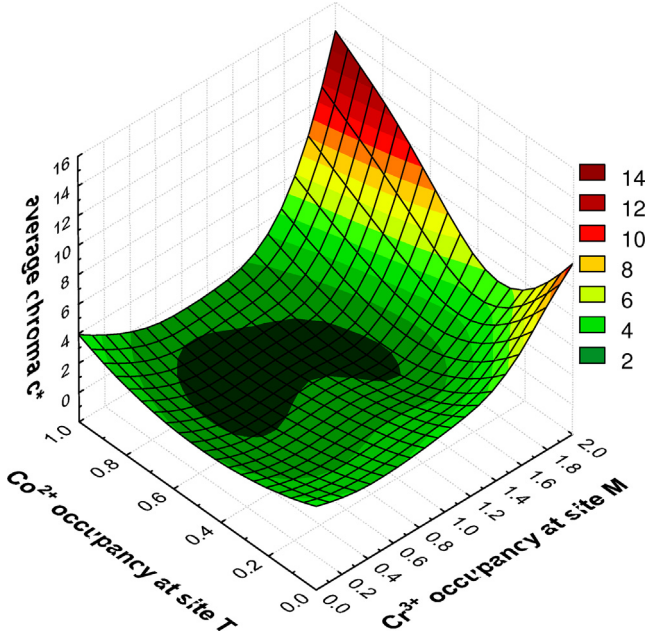

Fig. 11. Contour plot of chroma (C^*_{av}) averaged for the different glazes and glassy coatings under investigation versus Co^{2+} occupancy at site T and Cr^{3+} occupancy at site M.

peaks in well resolved Raman spectra and predominance of magnetic absorption in Mössbauer spectra (e.g., sample 6).

3.5.4. Colour bleaching

As expectable, a poor performance is related to spinel dissolution in the melted glaze or glassy coating (or by phase transformation). As a matter of fact, P varies from 18% (sample 8) to 48% (sample 7). Colour bleaching is conspicuous when chromium is absent, indicating an insufficient firing stability of low-chromium formulations. It happened also for the sample 10, besides the Cr^{3+} saturation of the octahedral site and its as-synthesized black colour, because of the occurrence of eskolaite—hematite that is not stable once applied in glazes (Fig. 9).

3.5.5. Glaze bloating

The bloating of glaze is another cause of unsuitable behaviour of pigments, despite their deep black colour [66]. It occurred in spinels exhibiting a high amount of Mn^{3+}: 0.64 apfu in the sample 13 or 1.0 apfu for samples 5 and 8 (Table 1). However, the occurrence of trivalent manganese is not detrimental by itself: for example in the sample 12, displaying the best technological behaviour, $^{VI}Mn^{3+}$ is as high as 0.33 apfu. Nevertheless, colouring performance worsens significantly when Mn^{3+} concentration is increased to 0.5 apfu (samples 14 and 15). Therefore, the threshold may be put around 0.6 apfu, a value that must not be overcome to avoid bloating phenomena (but best should be not passing 0.4 apfu). Bloating derives from reactions evolving gases and/or lowering the melt viscosity: both causes might be linked to the pigment persistence. In fact, trivalent manganese in spinel could be unstable in contact with glaze during ceramic firing; its reduction may lead to oxygen evolution: $2\ ^{M}Mn^{3+}+2e^{-}\rightarrow 2\ ^{M}Mn^{2+}+V_O$, implying the formation of oxygen vacancies (Vo). As a matter of fact, high valence manganese oxides (e.g. MnO_2)

are commonly used as oxidizing agents in the glass and ceramic industry [67].

Once spinel is dissolved, it changes the glaze composition and hence its physical properties, like viscosity at high temperature. Increasing the amount of spinel dissolved in the glaze causes a lowering of glaze viscosity (Fig. 12). Every sample here considered might play as a flux, with a more pronounced effect of pigment 8, whose limited persistence induced an estimated reduction of glaze viscosity around 7%, that can eventually explain the bloating phenomena. In contrast, the glazes containing samples 6, 11 and 12 have their viscosity lowered by no more than 1%, so not enough to cause bloating. However, the glazes containing the pigments 5 and 13 are not affected by a strong viscosity drop (about 2%) thus redox reactions involving manganese ions have to be invoked to explain bloating.

3.5.6. *Crystal structure and chemistry after firing*

An important aspect, disclosed here for the first time in ceramic pigments, is that the spinel lattice parameter turns systematically smaller after the ceramic processing (Table 6). The difference of unit cell length between the as-synthesized spinel (a_{as}) and the same after firing (a_{af}) is $0.012 < a_{as}—a_{af} < 0.043$ Å, therefore greater enough than the experimental error to make this observation reliable. As the unit cell parameter depends on the average cationic size [7,8], this contraction must reflect a significant change in the crystal chemistry of spinels. It implies that the concept of resistance to corrosion of spinel involves the ability to adjust its composition without losing colouring strength. In as-synthesized spinels, both sites are predominantly occupied by the smallest ions ($^{IV}Co^{2+}$ and $^{VI}Cr^{3+}$) among those possibly occurring in the Co—Cr—Fe—Mn system [8]. From this standpoint, no change in the partition of octahedrally-cordinated cations can justify such a unit cell contraction, as the bond distance of Cr^{3+} (1.995 Å) is shorter than those of Fe^{3+} (2.025 Å), Mn^{2+} (2.191 Å) and Mn^{3+} (2.03 Å). The same is for tetrahedrally-cordinated cations, as the T-O distance of Co^{2+} (1.972 Å) is lower than those of Mn^{2+} (2.036 Å) and Fe^{2+} (2.000 Å) with the exception of Fe^{3+} (1.875 Å). On the other hand, pigments got in touch with a melt that contains elements with a high affinity for the spinel lattice, like aluminium, magnesium and zinc. At any rate, the only cation with a small radius that is abundant in glazes and at the same time can be readily accommodated in both sites of the spinel lattice is the Al^{3+} (whose bond distance is 1.774 and 1.908 Å when fourfold- and sixfold-coordinated, respectively). Magnesium may be found in both crystallographic sites, but its bond distances are longer than Cr–O ($^{VI}Mg^{2+}$—O = 2.082 Å) or too close to that of cobalt ($^{IV}Mg^{2+}$—O = 1.966 Å) to explain the observed lattice parameters. Analogous consideration can be done about Zn^{2+}, that is normally hosted at the tetrahedral site ($^{IV}Zn^{2+}$—O = 1.96 Å); at any rate, it is absent in the glaze S1 and it would have a marked effect on colour [2—5]. Therefore, the smaller unit cell parameter of spinels after ceramic firing (a_{af}) could be justified by an Al^{3+} substitution after, e.g., Mn^{3+} and/or Fe^{3+} at the octahedral site. In the case of spinels listed in Table 6, the following equation was used to estimate the spinel lattice parameter [8]:

$$a = 8/11\sqrt{3}\{5T{-}O + [33(M{-}O)^2 — 8(T{-}O)^2]^{0.5}\}$$

by means of the average tetrahedral T–O and octahedral M–O bond distances. By this way, the amount necessary to lower the lattice parameter to the value measured in glazes is $0.23 < {}^{VI}Al^{3+} < 0.29$ apfu, though for samples 6 and 8 is 0.13—0.14 apfu. This amount of sixfold-coordinated aluminium has a limited effect on the spinel optical properties and should be low enough to be achieved even in the fast firing cycles used in tilemaking. Further studies are needed to understand how spinels change their composition in touch with melted glazes.

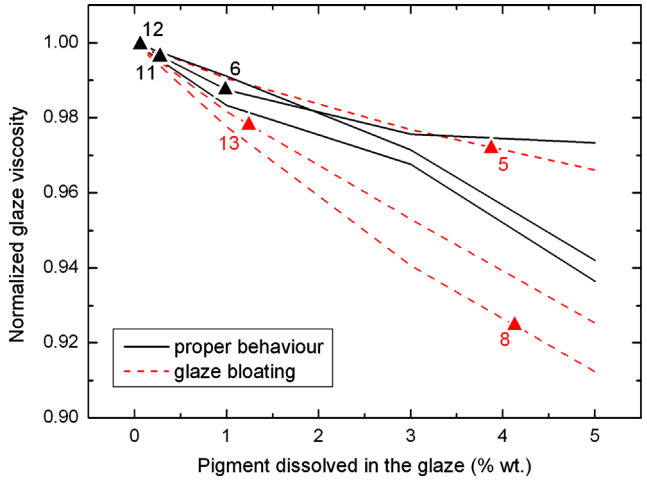

Fig. 12. Glaze viscosity at the maximum firing temperature in function of the amount of pigment potentially dissolved in the glaze. Triangles represent the actual amount of pigment dissolved. Best performing samples (6, 11 and 12) are compared with bloating samples (5, 8 and 13).

4. Conclusions

The cation distribution in as-synthesized spinels apparently follows an overall pattern governed by Co^{2+} occupancy of T site and Cr^{3+} occupancy of M site, with Mn^{3+} hosted at M site, Fe^{2+} at T site (only in the case of reducing firing atmosphere) while Mn^{2+} and Fe^{3+} are distributed over both sites. Nevertheless, despite the spinel unit cell and inversion parameters define a relatively narrow field in between "chromites" and "magnetites", Raman and Mössbauer data attest an increasing degree of disorder in cation distribution going towards the iron-rich terms, where clusters richer in Fe might be dispersed in a spinel matrix less rich in Fe.

The technological behaviour of spinel pigments is strongly connected with their crystal chemistry, with no significant effect by grain/crystallite size. The best colouring performance stems from an enhanced resistance to corrosion (by dissolution in the melted glaze and by change in spinel composition). The following ranges are recommended to get the best black pigments: Co^{2+} (0.4—0.8 apfu) together with Mn^{2+} (0.1—0.5) and Fe^{3+} (0.1—0.25) at T site; Cr^{3+} (0.9—1.5 apfu) together with Fe^{3+} (0.3—1.0), Mn^{3+} (0.1—0.5) and Mn^{2+} (≤0.21) at M site. These formulations are effective even if spinels undergo a change in their crystal chemistry as a consequence of oxidation and contact with melted glaze. As a matter of fact, a systematic decreasing of the unit cell

parameter occurs during firing, which is compatible with incorporation of 0.1—0.3 apfu of Al^{3+} at M site. Different pathways can give rise to excellent black pigments: (a) strongly disordered spinels hosting at least 7 transition metal cations and having an inversion parameter i~0.2 (Mn-bearing ternary and quaternary systems) and spinels where the sum Cr+Fe saturates the M site. These can be: (b) moderately disordered spinels, free of Mn^{3+}, having $i < 0.1$, or (c) apparently ordered and normal spinels halfway from cobalt chromite and cobalt ferrite.

Poor technological performances are due to different conditions, all limiting the resistance to corrosion of pigments: (i) a low amount of chromium (leaving room to colour bleaching); (ii) Mn^{3+} occupancy exceeding ~0.6 apfu (causing glaze bloating by redox reactions evolving gas and/or lowering glaze viscosity); (iii) oversaturation of site M by Cr+Fe: if the Fe^{3+} excess is < 0.3 apfu, a kenotetrahedral cationic arrangement is likely to occur; if this excess is > 0.3 apfu, an eskolaite—hematite solid solution exsolves (with a Cr/Fe ratio close to that of the batch).

Acknowledgments

The present work benefited from financial support of the Italian PRIN 2008 "SPIN GEO-TECH". Many thanks to Guia Guarini (ISTEC) for her assistance in technological testing.

References

[1] P. Escribano, J.B. Carda, E. Cordoncillo, Esmaltes y pigmentos cerámicos, Faenza Editrice Iberica, Castellon, 2001.
[2] Italian Ceramic Society, Colour, Pigments and Colouring in Ceramics, SALA, Modena, 2003.
[3] R.A. Eppler, Selecting ceramic pigments, American Ceramic Society Bulletin 66 (1987) 1600–1604.
[4] E. Ozel, S. Turan, Production and characterisation of iron—chromium pigments and their interactions with transparent glazes, Journal of the European Ceramic Society 23 (2003) 2097–2104.
[5] R.A. Eppler, Colorants for ceramics, in: R.E. Kirk, D.F. Othmer (Eds.), Encyclopedia of Chemical Technology, 8, Wiley, New York, 1998, pp. 877–892.
[6] G.N. Maslennikova, Pigments of the spinel type, Glass and Ceramics 58 (2001) 5–6.
[7] K.E. Sickafus, J.M. Wills, N.W. Grimes, Spinel compounds: structure and property relations, Journal of the American Ceramic Society 82 (1999) 3279–3292.
[8] B. Lavina, G. Salviulo, A. Della Giusta, Cation distribution and structure modelling of spinel solid solutions, Physics and Chemistry of Minerals 29 (2002) 10–18.
[9] A. Nakatsuka, Y. Ikeda, Y. Yamasaki, N. Nakayama, T. Mizota, Cation distribution and bond lengths in $CoAl_2O_4$ spinel, Solid State Communications 128 (2003) 85–90.
[10] H. O'Neill, W. Dollase, Crystal structures and cation distributions in simple spinels from powder XRD structural refinements: $MgCr_2O_4$, $ZnCr_2O_4$, Fe_3O_4 and the temperature dependence of the cation distribution in $ZnAl_2O_4$, Physics and Chemistry of Minerals 20 (1994) 541–555.
[11] CPMA, Classification and Chemical Description of the Complex Inorganic Color Pigments, 4th edition, Dry Color Manufacturers Association, Alexandria, 2010.
[12] K. Nassau, The Physics and Chemistry of Color, 2nd Edition, Wiley, New York, 2001.
[13] R.G. Burns, Mineralogical Applications of Crystal Field Theory, 2nd edition, Cambridge University Press, Cambridge, 1993.
[14] M. Wildner, M. Andrut, C.Z. Rudowicz, Optical absorption spectroscopy in geosciences. Part I: Basic concepts of crystal field theory, in: A. Beran, E. Libowitzky (Eds.), Spectroscopic Methods in Mineralogy, 6, Eötvös University Press, Budapest, 2004, pp. 93–144.
[15] E. Ozel, H. Yurdakul, S. Turan, M. Ardit, G. Cruciani, M. Dondi, Co-doped willemite ceramic pigments: technological behaviour, crystal structure and optical properties, Journal of the European Ceramic Society 30 (2010) 3319–3329.
[16] C. Zanelli, G. Guarini, M. Raimondo, M. Dondi, The vitreous phase of porcelain stoneware: composition, evolution during sintering and physical properties, Journal of Non-Crystalline Solids 357 (2011) 3251–3260.
[17] H. Yurdakul, S. Turan, E. Ozel, The mechanism for the colour change of iron chromium black pigments in glazes through transmission electron microscopy techniques, Dyes and Pigments 91 (2011) 126–133.
[18] F. Matteucci, C. Lepri Neto, M. Dondi, G. Cruciani, G. Baldi, A.O. Boschi, Colour development of red perovskite pigment $Y(Al,Cr)O_3$ in various ceramic applications, Advances in Applied Ceramics 105 (2006) 99–106.
[19] A. Escardino, S. Mestre, C. Feliu, P. Jodar, L. Dôaz, Stability of (Cr)CaO SnO_2 SiO_2 pink pigment in ceramic frits, British Ceramic Transactions 101 (2002) 213–220.
[20] M. Martos, M. Martínez, E. Cordoncillo, P. Escribano, Towards more ecological ceramic pigments: study of the influence of glass composition on the colour stability of a pink chromium-doped ceramic pigment, Journal of the European Ceramic Society 27 (2007) 4561–4567.
[21] Z. Mesíková, P. Šulcová, M. Trojan, Preparation and practical application of spinel pigment $Co_{0.46}Zn_{0.55}(Ti_{0.064}Cr_{0.91})_2O_4$, Journal of Thermal Analysis and Calorimetry 84 (2006) 733–736.
[22] D. Lenaz, H. Skogby, F. Princivalle, U. Hålenius, Structural changes and valence states in the $MgCr_2O_4$—$FeCr_2O_4$ solid solution series, Physics and Chemistry of Minerals 31 (2004) 633–642.
[23] G.B. Andreozzi, F. Princivalle, H. Skogby, A. Della Giusta, Cation ordering and structural variations with temperature in $MgAl_2O_4$ spinel: an X-ray single-crystal study, American Mineralogist 85 (2000) 1164–1171.
[24] G. Costa, V.P. Della, M.J. Ribeiro, A.P.N. Oliveira, G. Monrós, J.A. Labrincha, Synthesis of black ceramic pigments from secondary raw materials, Dyes and Pigments 77 (2008) 137–144.
[25] M.H. Aly, I.S. Ismael, F. Bondioli, Synthesis of coloured ceramic pigments by using chromite and manganese ores mixtures, Cerâmica 56 (2010) 156–161.
[26] W. Hajjaji, M.P. Seabra, J.A. Labrincha, Evaluation of metal-ions containing sludges in the preparation of black inorganic pigments, Journal of Hazardous Materials 185 (2011) 619–625.
[27] B. Tanişan, S. Turan, Black ceramic pigments for porcelain tile bodies produced with chromite ores and iron oxide waste, Journal of Ceramic Processing Research 12 (2011) 462–467.
[28] B. Tanişan, S. Turan, Synthesis of Fe—Mn black pigments by using hematite waste and manganese ore mixtures, Transactions of Indian Ceramic Society 71 (2012) 17–20.
[29] A.V. Zaichuk, Ya.I. Belyi, Black ceramic pigments based on open-hearth slag, Glass and Ceramics 69 (2012) 99–103.
[30] R.A. Eppler, Cobalt-free black pigments, American Ceramic Society Bulletin 59 (1980) (407—407).
[31] R.A. Eppler, Cobalt-free black pigments, American Ceramic Society Bulletin 60 (1981) 562–565.
[32] J.-H. Kim, S.-H. Lee, M.-C. Suh, B.-H. Lee, Synthesis of cobalt oxide free black color spinel pigment, Journal of the Korean Ceramic Society 44 (2007) 639–644.
[33] K.-H. Lee, M.-S. Myung, B.-H. Lee, Development of black color spinel pigment for high temperature, Journal of the Korean Ceramic Society 44 (2007) 160–165.
[34] K.-H. Shin, B.H. Lee, Synthesis of Fe_2O_3—CoO—Cr_2O_3—MnO_2 pigments and coloring in glazes, Journal of the Korean Ceramic Society 44 (2007) 554–561.
[35] K.-H. Lee, Y.-S. Lee, J.-S. Park, B.-H. Lee, Preparation and characterization of black zirconia ceramics by black color spinel pigment, Journal of the Korean Ceramic Society 45 (2008) 214–219.

[36] S. Mestre, M.D. Palacios, P. Agut, Solution combustion synthesis of (Co, Fe)Cr_2O_4 pigments, Journal of the European Ceramic Society 32 (2012) 1995–1999.
[37] M. Ye, A. Han, Z. Chu, J. Che, C. Wang, Synthesis and characterization of Mn-doped copper chromite black pigments, Advanced Materials Research 71 (2012) 602–604.
[38] J. Calbo, M.A. Tena, G. Monrós, M. Llusar, R. Galindo, J.A. Badenes, Flux agent effect on nickel ferrite black pigment, American Ceramic Society Bulletin (2005) 9201–9206.
[39] D. Gardini, M. Dondi, A.L. Costa, F. Matteucci, M. Blosi, C. Galassi, G. Baldi, E. Cinotti, Nano-sized ceramic inks for drop-on-demand ink-jet printing in quadrichromy, Journal of Nanoscience and Nanotechnology 8 (2008) 1979–1988.
[40] P.M.T. Cavalcante, M. Dondi, G. Guarini, M. Raimondo, G. Baldi, Colour performance of ceramic nano-pigments, Dyes and Pigments 80 (2009) 226–232.
[41] D. Verucchi, M. Cavedoni, Pigmented ceramic inks, Ceramic World Review 91 (2011) 66–69.
[42] M. Dondi, M. Blosi, D. Gardini, C. Zanelli, Ceramic pigments for digital decoration inks: an overview, cfi/DKG 89 (2012) E59–E64.
[43] A.F. Gualtieri, E. Mazzucato, P. Venturelli, A. Viani, P. Zannini, L. Petras, Determination of nickel(II) oxide in ceramic pigments by in situ X-ray diffraction quantitative analysis, Journal of the American Ceramic Society 82 (1999) 2566–2568.
[44] C.M.B. Henderson, J.M. Charnock, D.A. Plant, Cation occupancies in Mg, Co, Ni, Zn, Al ferrite spinels: a multi-element EXAFS study, Journal of Physics: Condensed Matter 19 (2007) 076214 (25pp).
[45] G.B. Andreozzi, U. Hålenius, H. Skogby, Spectroscopic active $^{IV}Fe^{3+}$—$^{VI}Fe^{3+}$ clusters in spinel—magnesioferrite solid solution crystals: a potential monitor for ordering in oxide spinels, Physics and Chemistry of Minerals 28 (2001) 435–444.
[46] A.C. Larson, R.B. Von Dreele, GSAS, general structure analysis system, Los Alamos National Laboratory, Los Alamos, Laur, 1988.
[47] B.H. Toby, EXPGUI, a graphical user interface for GSAS, Journal of Applied Crystallography 34 (2001) 210–213.
[48] A. Della Giusta, S. Carbonin, G. Ottonello, Temperature-dependent disorder in a natural Mg—Al—Fe^{2+}—Fe^{3+}-spinel, Mineralogical Magazine 60 (1996) 603–616.
[49] H. Sawada, Residual electron density study of chromium sesquioxide by crystal structure and scattering factor refinement, Materials Research Bulletin 29 (1994) 239–245.
[50] A.H. Hill, A. Harrison, C. Dickinson, W. Zhou, W. Kockelmann, Crystallographic and magnetic studies of mesoporous eskolaite, Cr_2O_3, Microporous and Mesoporous Materials 130 (2010) 280–286.
[51] E.N. Maslen, V.A. Strel'tsov, N.R. Strel'tsova, N. Ishizawa, Synchrotron X-ray study of the electron density in alpha Fe_2O_3, Acta Crystallographica B 50 (1994) 435–441.
[52] H. Sawada, An electron density residual study of alpha-ferric oxide, Materials Research Bulletin 31 (1996) 141–146.
[53] P. Schouwink, L. Dubrovinsky, K. Glazyrin, M. Merlini, M. Hanfland, T. Pippinger, R. Miletich, High-pressure structural behavior of alpha-Fe_2O_3 studied by single-crystal X-ray diffraction and synchrotron radiation up to 25 GPa, American Mineralogist 96 (2011) 1781–1786.
[54] M.P. O'Horo, A.L. Frisillo, W.B. White, Lattice vibrations of $MgAl_2O_4$ spinel, Journal of Physics and Chemistry of Solids 34 (1973) 23–28.
[55] A. Wang, K.E. Kuebler, B.L. Jolliff, L.A. Haskin, Raman spectroscopy of Fe—Ti-Cr—oxides, case study: Martian meteorite EETA79001, American Mineralogist 89 (2004) 665–680.
[56] M. Lazzeri, P. Thibaudeau, Ab initio Raman spectrum of the normal and disordered $MgAl_2O_4$ spinel, Physical Review B74 (2006) 140301.
[57] J.M. Malézieux, J. Barbillat, B. Cervelle, J.P. Coutures, M. Couzi, B. Piriou, Study of synthetic spinels of the $Mg(Cr_xAl_{2-x})O_4$ series and of natural chromites by Raman-laser microprobe, Tschermaks Mineralogische und Petrographische Mitteilungen 32 (1983) 171–185.
[58] H. Cynn, S.K. Sharma, T.F. Cooney, M. Nicol, High-temperature Raman investigation of order-disorder behavior in the $MgAl_2O_4$ spinel, Physical Review B45 (1992) 500–502.
[59] Z. Wang, P. Lazor, S.K. Saxena, G. Artioli, High-pressure Raman spectroscopic study of spinel ($ZnCr_2O_4$), Journal of Solid State Chemistry 165 (2002) 165–170.
[60] P. Chandramohan, M.P. Srinivasan, S. Velmurugan, S.V. Narasimhan, Cation distribution and particle size effect on Raman spectrum of $CoFe_2O_4$, Journal of Solid State Chemistry 184 (2011) 89–96.
[61] J. Preudhomme, P. Tarte, Infrared studies of spinels III: the normal II-III spinels, Spectrochimica Acta 27A (1971) 1817–1835.
[62] Z.V. Marinkovic Stanojevic, N. Romcevic, B. Stojanovic, Spectroscopic study of spinel $ZnCr_2O_4$ obtained from mechanically activated ZnO—Cr_2O_3 mixtures, Journal of the European Ceramic Society 27 (2007) 903–907.
[63] S.M. Yunus, H. Yamauchi, A.K.M. Zakaria, N. Igawa, A. Hoshikawa, Y. Ishii, Cation distribution and crystallographic characterization of the quaternary spinel system $Mg_xCo_{1-x}Cr_xFe_{2-x}O_4$, Journal of Alloys and Compounds 454 (2008) 10–15.
[64] G. Kullerud, G. Donnay, J.D.H. Donnay, Omission solid solution in magnetite: Kenotetrahedral magnetite, Zeitschrift für Kristallographie—Crystalline Materials 128 (1969) 1–17.
[65] F. Bosi, G.B. Andreozzi, V. Ferrini, S. Lucchesi, Behavior of cation vacancy in kenotetrahedral Cr-spinels from Albanian eastern belt ophiolites, American Mineralogist 89 (2004) 1367–1373.
[66] S.H. Murdock, R.A. Eppler, The interaction of ceramic pigments with glazes, American Ceramic Society Bulletin 68 (1989) 77–78.
[67] E. Rothman, M. Maicas, A. Kettani, Use of micronised pyrolusite (β-MnO_2) in fast fired ceramic tiles, in: QUALICER 98, 5th World Congress on Ceramic Tile Quality, Castellon, 1998.